Rare Metal Materials and Engineering
Volume 55, Issue 11, November 2026
Available online at www.rmme.ac.cn

Science Press

Cite this article as: Wang Runze, Tang Jincheng, Shan Xuepeng, et al. In-Situ Laser Alloying of Fe-30Mn Biodegradable Metal and Its Biological Research[J]. Rare Metal Materials and Engineering, 2026, 55(11): 2713-2726. DOI: https://doi.org/10.12442/j.issn.1002-185X.20250452.

ARTICLE

In-Situ Laser Alloying of Fe-30Mn Biodegradable Metal and Its Biological Research

Wang Runze[1], Tang Jincheng[1], Shan Xuepeng[1], Huang Zhaozhen[1], Li Sijing[1], Yan Ming[1,2]

[1] Department of Materials Science and Engineering, Southern University of Science and Technology, Shenzhen 518055, China; [2] Jiaxing Research Institute, Southern University of Science and Technology, Jiaxing 314031, China

Abstract: Block and Gyroid scaffold Fe-30Mn alloys were prepared by powder bed fusion with laser beam (PBF-LB) and in-situ alloying, and the effects of different printing parameters on the performance of specimens were studied. Results show that insufficient laser energy input during printing leads to inhomogeneous mixing of iron and manganese, which degrades the properties of the alloy. Excessively high energy input can cause manganese to vaporize, yielding a composition that deviates from the target. With optimized laser parameters, block specimens exhibiting a uniform Fe/Mn distribution can be obtained with an ultimate tensile strength of 644.67 MPa, an elongation of 21.61%, and a corrosion rate of 0.042 mm/a in simulated body fluid. Moreover, the resulting porous scaffold shows a porosity of 49.84%, a yield strength (0.2% offset) of 66.11 MPa, a compressive strength at 20% strain of 170.76 MPa, and an elastic modulus of 6.41 GPa. The results of indirect toxicity tests and cell adhesion tests show that the alloys have good biocompatibility. In conclusion, the Fe-30Mn alloy prepared by PBF-LB in-situ alloying holds promise for biodegradable human bone implants.

Key words: PBF-LB; in-situ alloying; biodegradable metal

1 Introduction

Fractured human bones require temporary support and fixation until the native bone has healed. In severe cases, an internal implant becomes necessary[1–2]. Conventional implants are typically fabricated from non-biodegradable materials, and these implants should be removed promptly after healing; otherwise, they can impede bone growth in children and cause various complications, such as inflammation and osteolysis caused by stress shielding[3–6]. Implant removal necessitates a second surgical procedure, risking additional trauma, negatively impacting the medical experience of patients, and thereby discouraging patients from choosing implant therapy[7]. Biodegradable implants obviate the need for second surgical procedure, as they are gradually resorbed by the body and gradually replaced as autologous bone tissue heals[8].

Biomaterials can be divided into metal materials, polymer materials, ceramic materials, and composite materials according to their composition. Metal materials usually have higher mechanical properties and fracture toughness, so they are more suitable for load-bearing structures than polymer materials and ceramic materials[9]. The corrosion products of biodegradable metals need to be non-toxic and harmless to the human body, or any adverse reactions elicited by degradation products can be neutralized through the homeostatic mechanisms of body. Consequently, Mg, Zn, Fe, and their alloys are widely investigated as biodegradable metals[10]. However, these pure metal materials always have some problems. Pure magnesium corrodes too rapidly, generating large volumes of hydrogen gas[11–12]. The mechanical properties of pure zinc are poor, which are difficult to meet the needs of implants[11–12]. Although pure iron material has the advantages of good mechanical properties and easy molding, the sluggish corrosion rate hinders its broader application[11–12]. In order to solve the problem of pure iron as implants, the element Mn is added to accelerate the corrosion rate. When the content of Mn exceeds 25%, the Fe-Mn alloy is almost composed of γ phase, and γ phase has diamagnetism, which

Received date: November 30, 2025
Foundation item: Shenzhen Medical Research Fund (D2402016); National Natural Science Foundation of China (52271032); Shenzhen Science and Technology Innovation Commission (JSGG20210420091802007)
Corresponding author: Yan Ming, Ph. D., Professor, Department of Materials Science and Engineering, Southern University of Science and Technology, Shenzhen 518055, P. R. China, E-mail: yanm@sustech.edu.cn

Copyright © 2026, Northwest Institute for Nonferrous Metal Research. Published by Science Press. All rights reserved.

addresses the magnetic resonance imaging compatibility issues associated with pure iron[10,13–14]. Raising the Mn content from 20wt% to 35wt% increases the maximum elongation of Fe-Mn alloys but reduces their yield strength[15]. The lower the Mn content, the faster the corrosion rate, which also means that the release of Mn ions becomes faster, and it will cause a greater inhibitory effect on cells. Thus, Fe-30Mn may possess a more suitable composition[14–16].

The high density and high modulus of dense Fe-Mn alloy implants can cause a stress shielding effect[4,17]. This problem can be solved by making scaffolds or porous materials. Moreover, the open implant structure allows body fluids to pass through the implant to transport substances. Meanwhile, host tissue can infiltrate the scaffold. An enlarged surface area inherent to porous scaffolds accelerates the corrosion kinetics of the material[18]. Additive manufacturing is therefore regarded as an ideal route for fabricating biomaterials featuring intricate lattices and patient-specific geometries[19–20]. Powder bed fusion with laser beam (PBF-LB), also termed selective laser melting (SLM), uses a CAD model to drive the laser to selectively scan and locally melt successive powder layers, building the component layer by layer[20]. Conventional manufacturing of porous alloys suffers from non-uniform pore distribution and predisposition to clogging, thereby failing to meet the stringent requirements of medical applications. Conversely, PBF-LB technique permits precise manipulation of complex porous implant structures to mimic human bone structure[21]. Nevertheless, PBF-LB typically demands tailored pre-alloyed powders for non-standard composition, thereby inflating production costs[22]. In-situ alloying employs the laser to melt blended metal powders and complete the preparation of the alloy directly in the powder bed[22]. In PBF-LB, temperature or compositional gradients across the melt pool generate surface-tension-driven Marangoni convection. The resulting Marangoni force propels the melt radially outward, inducing upward flow at the pool center and downward flow on the surface. This fluid circulation draws the unmelted powder into the melt pool to promote powder melting, improves the diffusion process of the material, and ensures the composition uniformity of the material prepared by in-situ alloying[22–23]. In-situ alloying can use common powders instead of pre-alloyed powders as raw materials for PBF-LB, reducing production costs while enabling flexible custom alloy composition fabrication. It also enables the preparation of unconventional alloys and functionally graded materials[22].

Therefore, pure Fe and Mn powders were mixed and processed via PBF-LB in-situ alloying to prepare both block and Gyroid scaffold specimens. Their mechanical performance and indirect cytotoxicity were subsequently assessed.

2 Experiment

2.1 Materials

Spherical pure Fe powder (the diameter of 15–53 μm) and irregular pure Mn powder (the diameter of 15 – 53 μm) provided by Hebei Paian Technology Co., Ltd (China) were used as raw materials for PBF-LB. The chemical composition of the powders is provided by the supplier in Table 1. A TURBULA® three-dimensional shaker-mixer was employed to homogenize a mixture of 70wt% spherical Fe and 30wt% irregular Mn powders to obtain the Fe-30Mn mixed powder for PBF-LB in-situ alloying. Mixing was conducted for 1 h.

2.2 PBF-LB process

The blocks and Gyroid scaffolds of Fe-30Mn were prepared on HY-M150 (Huayang, China) PBF-LB system. The laser wavelength was 1060–1100 nm, the diameter was 100 μm, the hatching space was 100 μm, and the layer thickness was 30 μm. During the printing process, the substrate temperature was maintained at 200 °C, and the atmosphere of the working chamber was pure Ar. For the block specimens, including the tensile test specimens, the key parameters were: (1) laser power of 100–250 W at a fixed scanning speed of 800 mm/s; (2) scanning speed of 400–1200 mm/s at a fixed power of 150 W. For the Gyroid scaffold specimens, including the compression test specimens, the approximate strut thickness was 0.5 mm, the unit cell dimensions were 2.5 mm×2.5 mm×2.5 mm, the key parameters were: (1) the power of 120–210 W; (2) scanning speed at 600–1500 mm/s.

2.3 Materials characterization

The density of each block specimen was measured with a density balance. These values were compared with the theoretical density of Fe-30Mn (7.872 g/cm^3) to calculate the relative density[24]. Gyroid scaffold specimens were analyzed by micro-CT (Diondo d2, Germany) to determine relative density, specific surface area, and porosity.

The surfaces of both block and scaffold specimens were examined with a ZEISS Merlin scanning electron microscope (SEM, Carl Zeiss AG, Germany) equipped with an energy dispersive spectrometer (EDS). Before the observation, the block specimens were etched by 2% alcohol nitrate solution, and the Gyroid scaffold specimens were etched by phosphoric and citric acid solution to remove the surface dust.

2.4 Mechanical property test

Tensile and compression tests were conducted on an INSTRON 68TM-30, with three specimens per group. Schematic diagrams of the size of block tensile specimen and Gyroid scaffold compression specimen are shown in Fig.1.

2.5 Corrosion rate test

2.5.1 Block specimen

The size of block specimen was 14 mm×14 mm×5 mm. Electrochemical measurements were performed with a CorrTest workstation. A three-electrode cell (SCE as reference electrode, specimen as working electrode, and Cu as counter electrode) was employed in a simulated body fluid at 25 °C to

Table 1 Chemical composition of Fe and Mn powders (wt%)

Powder	Si	S	P	C	Fe	Mn
Pure Fe	0.004	0.011	0.0015	0.012	Bal.	0.001
Pure Mn	0.008	0.015	0.0019	0.008	0.050	Bal.

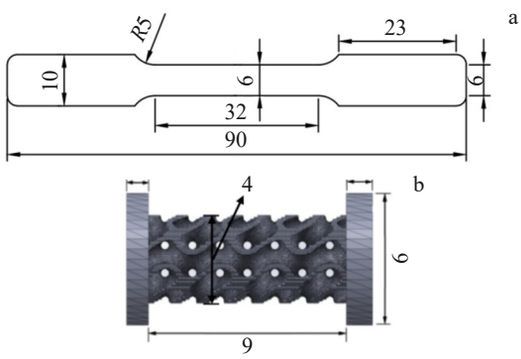


Fig.1 Schematic diagrams of the size of the block tensile specimen (a) and Gyroid scaffold compression specimen (b)

measure the potential dynamic polarization curve. The scanning range is from −1 V to 1 V, and the scanning rate is 1 mV/s. The chemical composition of the simulated body fluid is shown in Table 2, where the solvent was water. After dissolving the above reagents, hydrochloric acid was used to titrate the pH to 7.4. Corrosion rates were obtained by Tafel fitting the potential curve using the CorrTest workstation software.

2.5.2 Gyroid scaffold specimen

Cylindrical Gyroid specimens with the radius of 5 mm and the height of 4 mm were prepared for immersion testing. Corrosion rate was tested using the mass-loss method. Initial mass (m_1) was recorded before immersion in the simulated body fluid, whose chemical composition is shown in Table 2. The immersion time is t. After immersion, surface products were removed with citric acid-phosphoric acid solution, and the specimens were weighed to obtain the mass m_2. The simulated body fluid was renewed every 48 h. The final corrosion rate (CR) was calculated according to Eq. (1):

$$\mathrm{CR}=\frac{8.71\times10^4\left(m_1-m_2\right)}{A\rho t} \quad (1)$$

where A is the surface area measured by micro-CT, ρ is the density measured by micro-CT, and t is the immersion time.

2.6 Cytotoxicity test

For block specimens, cylindrical specimens (14 mm in diameter and 4 mm in height) were ultrasonically cleaned in acetone followed by absolute ethanol. After air-drying and sterilization, the specimens were cultured in DMEM medium for 24 h. The extraction medium, which conformed to ISO-10993-12 standard[25], was filtered and supplemented with 1% penicillin-streptomycin and 10% fetal bovine serum, and the resulting conditioned medium was used for all subsequent experiments. Gyroid scaffold specimens (10 mm in diameter and 4 mm in height) were treated identically. The cylindrical pure iron with the same size was used as the control group for both block and Gyroid Fe-30Mn specimens.

Table 2 Chemical composition of the simulated body fluid (1000 mL)

Chemical composition	Mass/g
NaCl	8.000
$NaHCO_3$	0.350
KCl	0.224
$K_2HPO_4\cdot3H_2O$	0.167
$MgCl_2\cdot6H_2O$	0.305
$CaCl_2$	0.278
Na_2SO_4	0.071

MG-63 cells were used for indirect cytotoxicity test. Extracts obtained from block specimens were diluted at a ratio of 1:2 using fresh medium. MG-63 cells were seeded into 96-well plates at a concentration of 1×10^4 cells per well, and the prepared medium was added to each well. At the same time, the holes filled with complete medium were set as negative control group. Each group contained three replicate wells. The plates were incubated at 37 °C in 5vol% CO_2. After 1, 3, and 5 d, the original medium was removed. Complete medium containing 10vol% CCK-8 solution was added, followed by incubation for 1 h. After 1 h, plates were gently shaken for 15 min. The optical density (OD) of each well at wavelength of 450 nm was measured using the microplate reader. Finally, the relative growth rate (RGR) was calculated as follows:

$$\mathrm{RGR}=\frac{\text{OD value of alloy sample}}{\text{OD value of control group}}\times100\% \quad (2)$$

Cytotoxicity test results were analyzed using one-way ANOVA in SPSS 17.0 (SPSS, Chicago, IL, USA) and were presented as mean±standard deviation. Statistical values were obtained from experiments that were conducted in triplicate at minimum. Statistical significance was set at $p<0.05$.

2.7 Cell adhesion test

Sterilized cylindrical specimens (14 mm in diameter and 4 mm in height) were placed in 24-well plates and seeded with MG-63 cells (4×10^4 cells per well) onto the surface of the specimen. After pre-incubation at 37 °C for 30 min, complete medium was added and cells were incubated at 37 °C for 2 h. Cells were washed three times with phosphate-buffered saline (PBS) and fixed at 4 °C for 12 h with 0.25% glutaraldehyde solution. After washing three times with PBS solution, the specimens were dehydrated using a graded ethanol series (10vol%, 30vol%, 50vol%, 70vol%, 80vol%, 90vol%, 95vol%, and 100vol%), with each concentration maintained for 10 min. Finally, the specimens were freeze-dried and sputter-coated with gold for SEM observation.

3 Results

3.1 Powder morphology

Fig. 2 presents the morphologies of spherical Fe powder, irregular Mn powder, and the Fe-30Mn mixture. EDS element mappings (Fig. 2d–2f) reveal a homogeneous distribution of Fe and Mn, which can ensure the uniformity of powder during PBF-LB printing.

3.2 Block specimen characterization

3.2.1 Surface morphology

After etching with 2% alcoholic nitric acid, the metallographic cross-sections of the block specimens display three distinct corrosion patterns (Fig. 3a–3c). The Fe-rich zones consist

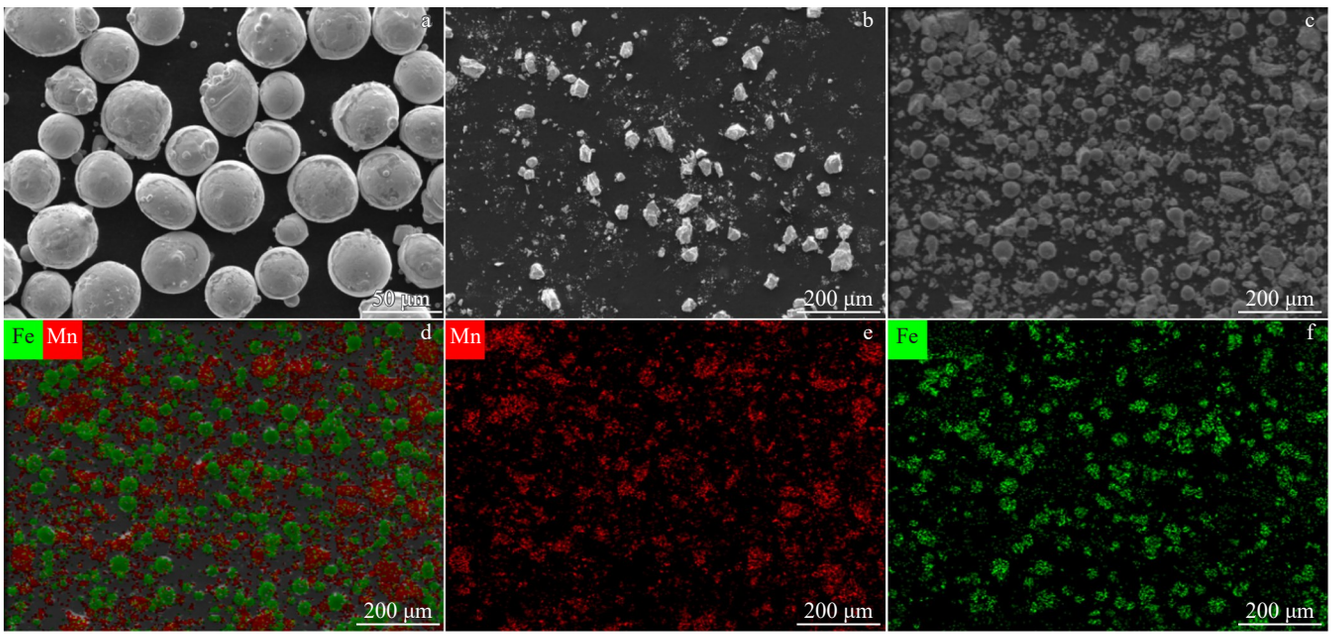


Fig.2 SEM images of spherical Fe powder (a), irregular Mn powder (b), and mixed Fe-30Mn powder (c); EDS element mappings of mixed Fe-30Mn powder (d), Mn distribution (e), and Fe distribution (f)

exclusively of Fe and exhibit flat surfaces traversed by fine vertical striations under SEM; corresponding EDS element mappings show dense green pixels. Mn-rich zones are porous and rough, appearing as closely packed red pixels in EDS element mapping. Intermediate zones contain both Fe and Mn, producing a scaly microstructure, which are composed of staggered and overlapping green pixels and red pixels. Given an identical etchant, zones with higher corrosion rates exhibit rougher metallographic surface. In Fe-rich zones, the surface remains flat, and fine polishing scratches are still visible. This indicates that the region underwent negligible corrosion. The scaly microstructure of the intermediate zones results from mild selective corrosion at grain boundary. Under mild corrosion, attack is preferentially localized at grain boundaries. Consequently, grain-boundary outlines are sharply delineated. The Mn-rich region exhibits severe corrosion, evidenced by deep intergranular grooving and pitting. In addition, severe corrosion creates deep grooves, and some grains are detached, generating pits.

The three corrosion patterns described above reflect the quality of PBF-LB in-situ alloying. Rough surface indicates poorly optimized laser parameters and poor compositional uniformity. The specimen prepared at low energy density (100 W, 800 mm/s) exhibits pores and corrosion pits on the surface in Fig. 3d. This phenomenon indicates that insufficient energy impedes complete melting and prevents homogenization of Fe-30Mn alloy. However, Fig. 3e and 3g present the surface morphology and corresponding EDS element mapping of specimen prepared with optimal parameters (150 W, 900 mm/s), respectively. The flat surface and uniform Fe/Mn distribution demonstrate that homogeneous Fe-30Mn alloy forms when appropriate parameters are applied. Moreover, EDS quantification result confirms 70.72wt% Fe and 29.28wt% Mn, with no significant deviation. This indicates minimal Mn loss, preserving the target Fe-30Mn composition. It is worth noting that at excessively high laser energy density, especially higher power (250 W, 800 mm/s), Mn content decreases. Fig. 3f and 3h reveal diminished Fe/Mn uniformity; EDS quantification result indicates 74.38wt% Fe and only 25.62wt% Mn. Additionally, Mn deposits are found on the chamber walls of PBF-LB machine after high-energy-density printing. This results from Mn vaporization followed by condensation on the chamber walls. Thus, the reduced Mn content may be attributable to excessively high energy input.

3.2.2 Relative density and corrosion rate

Fig. 4a–4b show that relative density rises with laser power up to 200 W, beyond which it falls; the corrosion rate drops steeply at first and then plateaus. Increasing scanning speed reduces relative density and yields a fluctuation, yet generally rising corrosion rate.

These relative density variations arise because higher energy input (via increased power or reduced scanning speed) enhances powder melting and flowing in the molten pool. Greater melt fluidity enables more effective void filling between Fe and Mn powders, increasing the particle packing density. Increased void filling lowers porosity and thus raises relative density. Consequently, the moderate increase in power or decrease in scanning speed can improve relative density of alloy. However, excessively high energy (over 200 W) will vaporize the low-boiling-point Mn powders, generating pores to cause lower relative density. This phenomenon has also been found in other related studies[26]. The block specimen prepared with optimal parameters exhibits relative density of 99.36%.

Combined with the results in Section 3.2.1, low laser energy (<150 W) enlarges Fe-rich and Mn-rich zones, fostering local galvanic couples and markedly accelerating

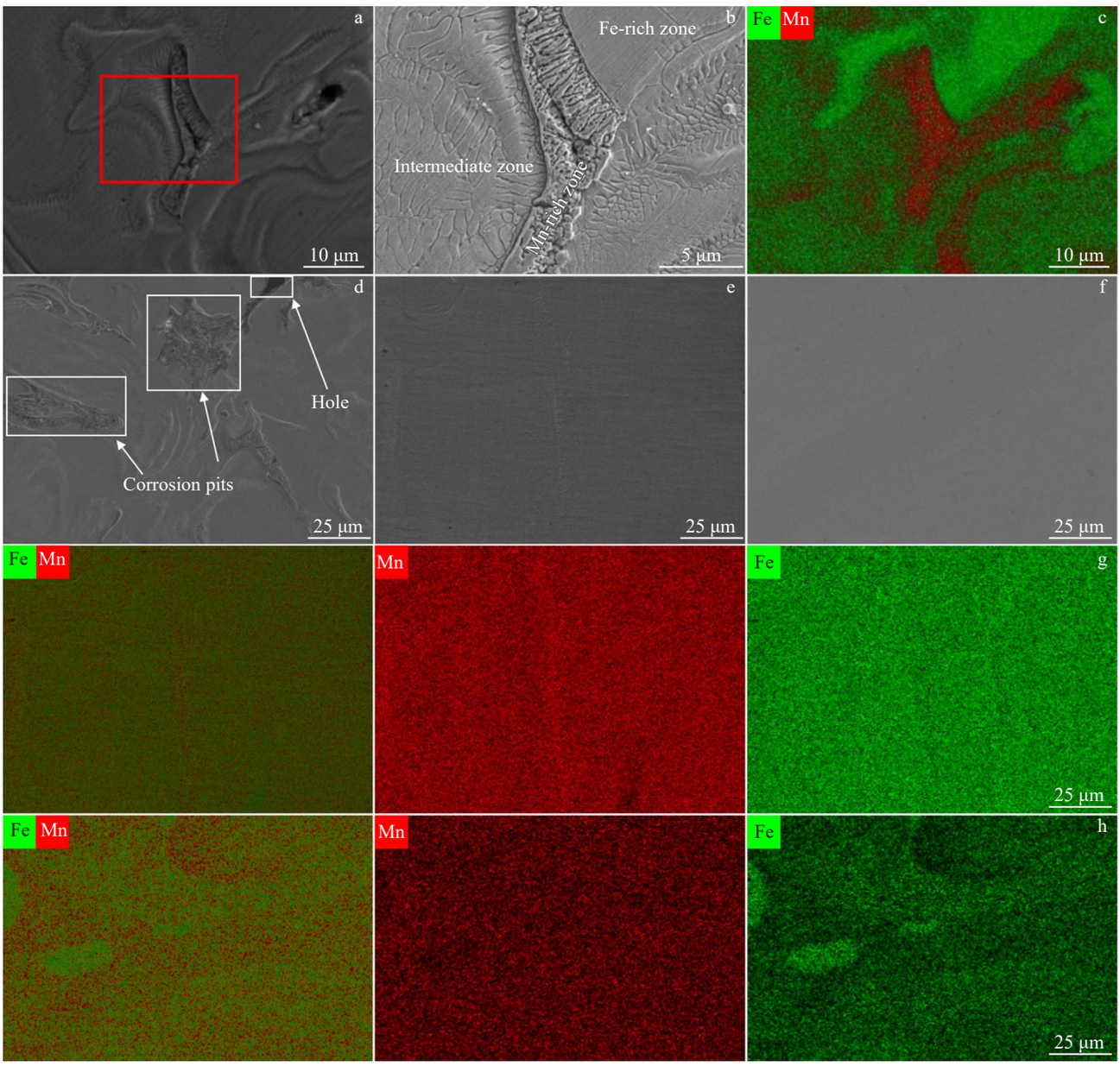


Fig.3 Corrosion morphologies of Fe-30Mn alloy (a–b); EDS element mapping corresponding to Fig. 3a (c); surface morphologies of Fe-30Mn specimens prepared with different laser parameters: (d) 100 W, 800 mm/s, (e) 150 W, 900 mm/s, and (f) 250 W, 800 mm/s; EDS element mappings corresponding to Fig.3e (g) and Fig.3f (h)

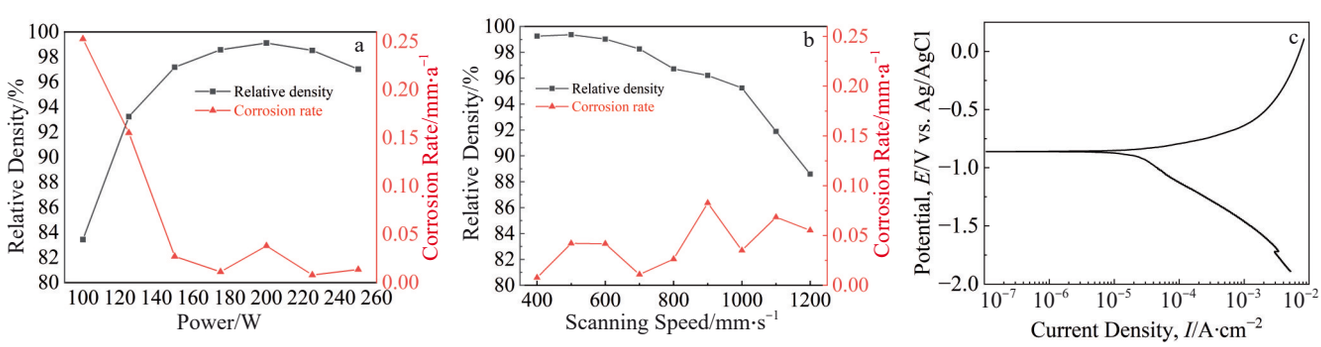


Fig.4 Effect of power (a) and scanning speed (b) on the relative density and corrosion rate; potential polarization curve of the block specimen at the laser power of 150 W and scanning speed of 500 mm/s (c)

corrosion relative to other parameter sets. Instrumental errors and other factors, however, introduce variability, resulting in the evident fluctuations observed in Fig. 4. It can be inferred that at medium or high laser energy density, corrosion rates

reach a plateau; this plateau may be attributed to density variations. Higher relative density reduces porosity and causes smaller surface area. Therefore, the corrosion rate tends to be low. According to the potential polarization curve shown in Fig. 4c, the corrosion rate of the specimen is 0.042 mm/a by Tafel fitting. This value lies within the recommended range of 0.04–0.14 mm/a for biodegradable implants in orthopedic and trauma surgery applications[27–28]. Specimens prepared with low and high energy densities both exhibit corrosion rates that lie within or very near to this range.

3.2.3 Mechanical properties

Fig. 5 summarizes the ultimate tensile strength (UTS) and elongation of the block specimens printed under six parameter sets. UTS and elongation both rise with the increase in laser power and decline as scanning speed increases. This trend reflects reduced energy density input at lower power or higher scanning speed, which causes incomplete in-situ alloying and poor powder melting, generating numerous pores. These pores act as internal defects. Consequently, UTS and elongation decrease under low power or high scanning speed.

Table 3 compares the mechanical properties of the block specimens with literature data. The specimens prepared in this study exhibit outstanding UTS and elongation, with an UTS of 644.67±12.13 MPa and an elongation of 21.61%±0.81%. Compared with Fe-30Mn alloys prepared by powder metallurgy, PBF-LB specimens display superior UTS and elongation, which meet the elongation requirement and exceed UTS criterion for orthopaedic internal fixation devices by more than twice.

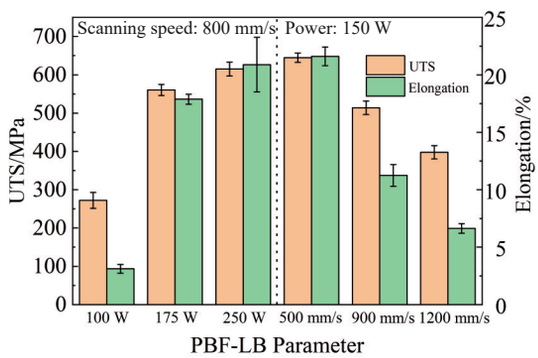


Fig.5 UTS and elongation of block specimens prepared with different laser parameters

Table 3 Comparison of mechanical properties between different materials[14,27]

Specimen	UTS/MPa	Elongation/%	Ref.
Fe-30Mn	644.67±12.13	21.61±0.81	This study
Fe-20Mn	702±11	7.5±1.5	[14]
Fe-25Mn	723±19	4.8±0.4	[14]
Fe-30Mn	518±14	19.0±1.4	[14]
Fe-35Mn	428±7	32.0±0.8	[14]
Criterion for orthopedic internal fixation device	>300	>18	[27]

Note: the Fe-20Mn, Fe-25Mn, Fe-30Mn, and Fe-35Mn alloys are prepared by powder metallurgy.

3.2.4 Indirect cytotoxicity

Fig. 6 illustrates the influence of laser power and scanning speed on the indirect cytotoxicity of the Fe-30Mn specimens. In general, higher laser power or slower scanning speed increases the RGR of the Fe-30Mn alloy compared with that of pure Fe. Most specimens exhibit RGR values below 100%, indicating marginally higher cytotoxicity than that of pure Fe with a statistically significant difference. However, for the Fe-30Mn specimen prepared at 150 W and 500 mm/s, RGR results exhibit no statistically significant difference from those of pure Fe after tests for 1 and 5 d, and RGR reaches 105.14% after 5 d, which means the indirect cytotoxicity of this specimen may be close to that of pure Fe.

This trend stems from the extent of Fe-Mn powder melting. Low power or high scanning speed can reduce the alloying degree of Fe-Mn specimen, leading to heterogeneous surface chemistry and pronounced Mn enrichment. Because Mn is more electrochemically active, Mn-rich zones release more Mn ions than fully alloyed zones. Excessive Mn ions exert cytotoxic effects that suppress cell proliferation, leading to low RGR values. With optimized laser parameters, Mn ion release is restrained. RGR value of the specimen reaches 105.14%±17.57% after 5 d, which means the cytotoxicity is slightly better than that of pure Fe.

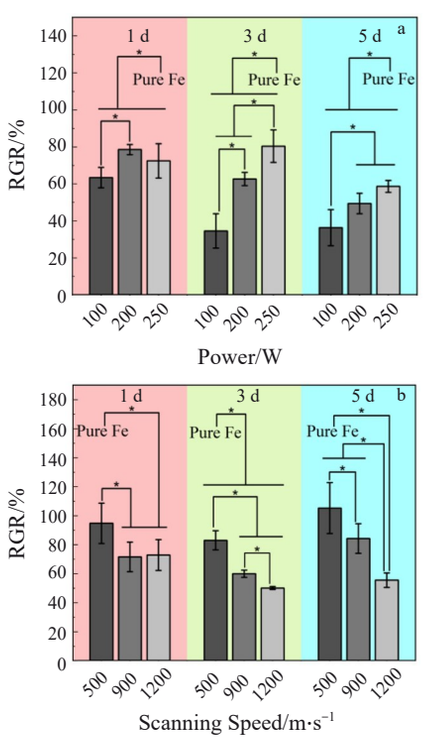


Fig.6 Effects of laser power (a) and scanning speed (b) on RGR of Fe-30Mn specimen compared with pure Fe (the scanning speed in Fig.6a is 800 mm/s, and the power in Fig.6b is 150 W)

3.2.5 Cell adhesion

Fig.7a shows the cell adhesion performance of MG-63 cells on the block specimen (laser power of 150 W, scanning speed of 500 mm/s). Clear pseudopodia (Fig.7b–7c) confirm that the cells adhere well to the surface of the specimen.

3.3 Gyroid scaffold specimen characterization

Based on corrosion behavior, mechanical performance, and cytotoxicity, the three parameter sets listed in Table 4 were selected for further discussion.

3.3.1 Surface morphology

Fig.8a–8c show the surface morphologies of the specimen #3 with unmelted metal powder adhered to the scaffold surface. Unmelted residues consist predominantly of spherical Fe particles; Mn powder residues are negligible, indicating near-complete melting of Mn.

Fig. 8d–8e show the micro-CT results of the specimen #3. The micro-CT scanning results also confirm that there is powder adhesion on the scaffold surface. In addition, the relative density of the specimen #3 is about 99.41%, the specific surface area is 3031.02 mm^2/g, and the porosity is 49.84%.

Table 4 Parameters of Gyroid scaffold specimens

Specimen	Power/W	Scanning speed/mm·s^{-1}
#1	120	600
#2	180	900
#3	210	600

3.3.2 Corrosion behavior

Fig. 9a – 9b show the morphologies of specimen #3 after corrosion for 14 d. The crystalline degradation products are visible. These products are analyzed by EDS, with composition results presented in Table 5. Although the exact composition varies among the points, all of them contain over 20wt% Mn, and no Fe is detected. Fig. 9c – 9d and the corresponding EDS results in Table 6 reveal that Fe and Mn precipitates simultaneously. Collectively, the above data

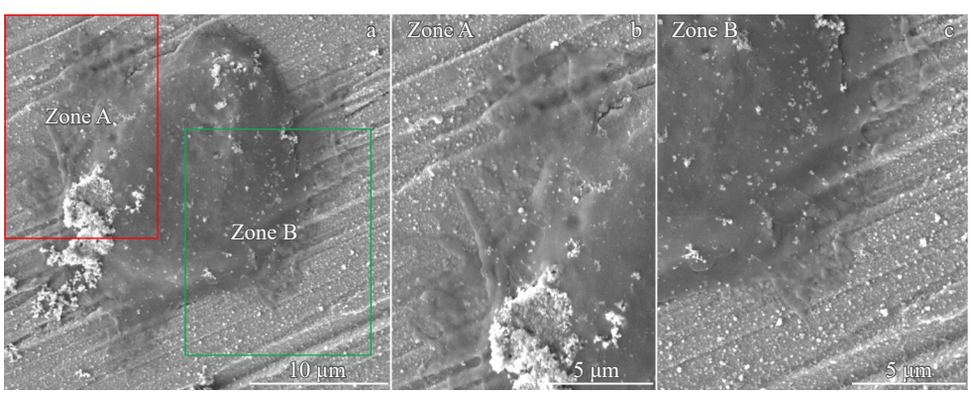


Fig.7 Cell adhesion image of block specimen (a); local magnified images with clear pseudopodia of zone A (b) and zone B (c) marked in Fig.7a

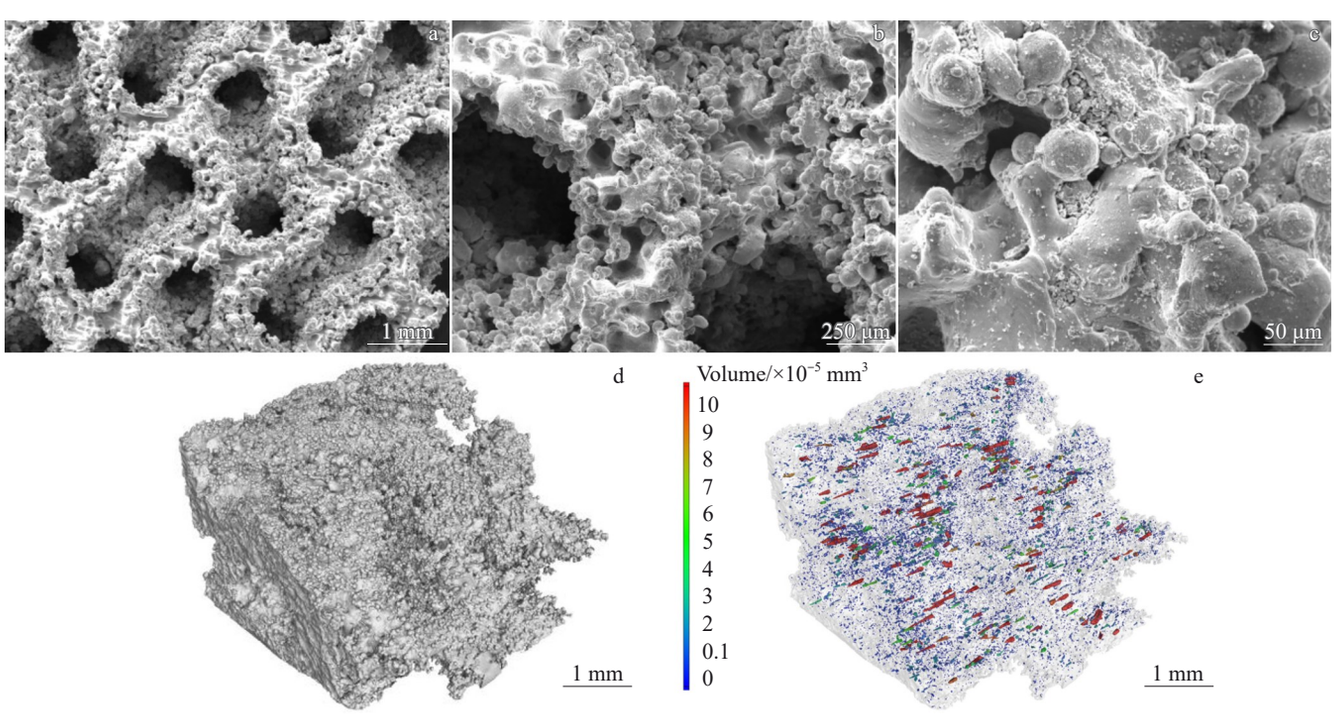


Fig.8 SEM surface morphologies (a–c), 3D micro-CT image (d), and pore distribution (e) of specimen #3

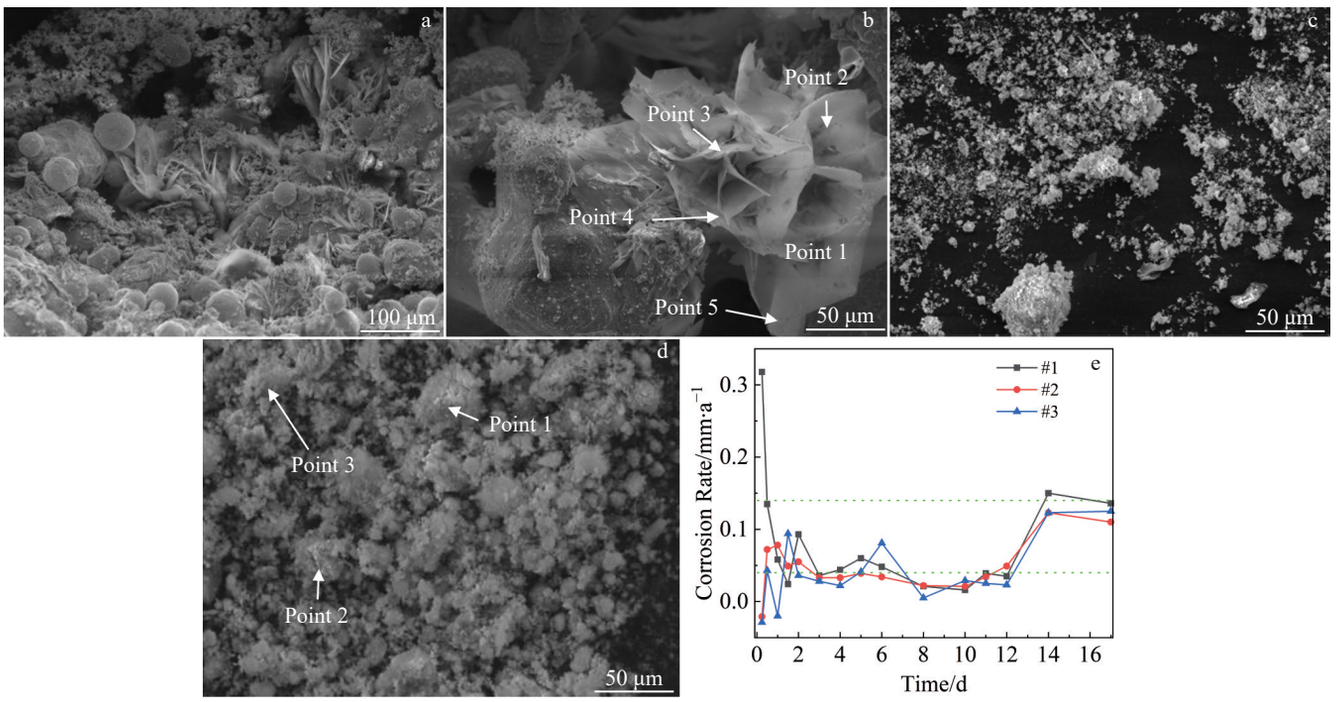


Fig.9 SEM images of surface morphologies (a–b) and precipitations (c–d) of specimens #3 after corrosion for 14 d; corrosion rate curves of the three specimens (e)

Table 5 EDS results of different points marked in Fig.9b (wt%)

Point	C	O	Na	P	Cl	Ca	Mn
1	6.25	40.93	2.90	4.90	6.07	13.53	25.41
2	5.23	37.37	2.24	5.37	5.79	13.72	30.27
3	5.10	37.56	3.81	5.37	5.87	13.08	29.20
4	3.48	16.28	9.16	2.05	38.76	8.64	21.63
5	6.41	32.80	5.19	8.14	9.15	12.90	25.41

Table 6 EDS results of different points marked in Fig.9d (wt%)

Point	C	O	P	Ca	Mn	Fe
1	4.09	30.96	4.08	5.57	29.16	26.14
2	4.08	40.24	4.16	7.27	0	44.26
3	5.98	45.45	12.38	16.37	19.81	0

indicate that released Mn ions are partially adsorbed onto the scaffold surface, with the rest precipitating. In contrast, Fe ions are predominantly enriched in the bottom precipitation, instead of adhering to the scaffold.

Fig. 9e presents the corrosion rate curves for all three specimens. After 2 d, corrosion rates for all specimens lie within the range of 0.04–0.14 mm/a, satisfying the criterion for biodegradable implants[26–27]. Specimen #1 exhibits an initial decline in corrosion rate over the first 1.5 d before leveling off, whereas the corrosion rates of specimens #2 and #3 rise initially and then stabilize. Despite specimens prepared with different laser parameters, corrosion rates converge after approximately 3 d. For specimen #1, the rapid initial drop reflects low energy density and weak surface bonding, causing early alloy detachment. Consequently, corrosion rate is initially high but stabilizes once loosely bonded material is removed. Stronger surface bonding and a protective oxide film initially retard the corrosion rate of specimens #2 and #3. Corrosion rate accelerates gradually as the oxide film dissolves and then stabilizes.

3.3.3 Mechanical properties

Fig. 10 shows the compression mechanical properties of specimen #3. Stage 1 (initial loading to point 1) corresponds to elastic deformation. During stage 2 (point 1 to point 2), progressive pore collapse leads to pronounced macroscopic deformation. During stage 3 (point 2 to point 3), the pores continue to collapse. During stage 4 (point 3 to point 4), due to external forces, strut fracture and debris generation cause load changes, yielding pronounced curve fluctuations. During stage 5 (point 4 to the end of compression), the scaffold undergoes densification, and the curve becomes smooth, and the stress rises monotonically until full compaction is achieved.

Specimen #3 exhibits a yield strength (0.2% offset) of 66.11±1.44 MPa, a compressive strength of 170.76±8.36 MPa at 20% strain, and an elastic modulus of 6.41±0.85 GPa. Comparing the mechanical properties of the three specimens with human cortical and cancellous bones, as shown in Table 7, the specimen #3 prepared in this study can satisfy the mechanical requirements of both bone tissues, whereas specimens #1 and #2 meet those of cancellous bone alone.

3.3.4 Indirect cytotoxicity

ISO 10993-5 defines cytotoxicity into grades 0 to 5 based on RGR: grade 0 (≥100%), grade 1 (75%–99%), grade 2

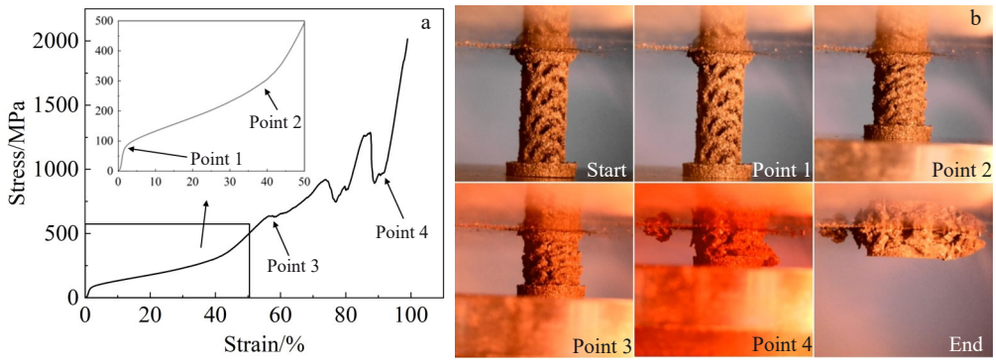


Fig.10 Stress-strain curves of specimen #3 (a); appearances of specimen #3 at different points marked in Fig.10a (b)

Table 7 Compression properties of different specimens

Material	Yield strength (0.2% offset)/ MPa	Compressive strength at 20% strain/MPa	Elastic modulus/GPa	Ref.
specimen #1	61.83±10.28	102.32±8.63	3.86±0.15	This study
specimen #2	55.59±4.06	104.31±6.51	4.37±0.7	This study
specimen #3	66.11±1.44	170.76±8.36	6.41±0.85	This study
Cortical bone	1–20	134^{+}	1–35	[29–30]
Cancellous bone	7.2–23.2^{+}	17–33^{+}	0.02–6	[29–30]

Note: the symbol $^{+}$ indicates that the specific strain value was not provided.

(50%–74%), grade 3 (25%–49%), grade 4 (1%–24%), and grade 5 (0%). Grades 0 and 1 indicate that the extraction is non-toxic. Fig. 11 shows RGR results of different specimens, which indicates that RGR values (75%–99%) of all three specimens fall within grade 1. Therefore, the specimen extraction is non-toxic and safe.

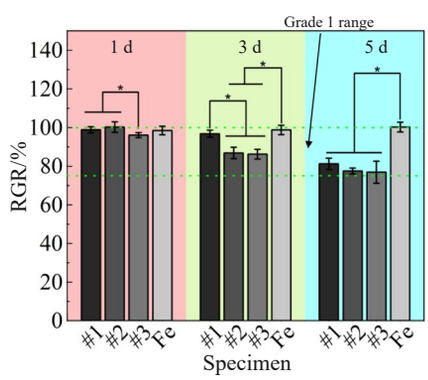


Fig.11 RGR results of different specimens

4 Discussion

4.1 In-situ alloying uniformity

SEM images and EDS results above demonstrate that simple mechanical mixture of spherical Fe and irregular Mn powders yields homogeneous feedstock suitable for PBF-LB. Even when spherical Fe powder and irregular Mn powder are employed, they can be thoroughly mixed without significant elemental enrichment, thus ensuring uniform elemental distribution across the powder bed during PBF-LB process.

Careful selection of laser parameters is crucial. PBF-LB in-situ alloying method with optimized laser parameters successfully prepared dense Gyroid scaffold Fe-30Mn specimen (relative density of 99.41%) with homogeneous Fe-Mn composition (70.72wt% Fe, 29.28wt% Mn) and negligible Mn loss. It is difficult to obtain specimens with high relative density when input laser energy is insufficient, including insufficient power or excessively high scanning speed. Insufficient laser energy restricts the fluidity of melt, especially that of the Fe powder, which has higher melting point, impeding thorough flow and mixing of Fe and Mn before the melt pool solidifies. Consequently, the as-built Fe-30Mn alloy (Fig.3b) exhibits pronounced Fe-rich and Mn-rich zones, which appear after etching.

However, excessively high energy density (particularly at high laser power) leads to unexpected specimen composition. The Mn content in the specimens decreases. Fig.12 shows the resulting images after the grayscale conversion and subsequent brightness and contrast modification of the EDS images in Fig.3g–3h. Throughout the transformation, identical elements in different specimens underwent identical processing, so the brightest pixel of each element retains the same intensity. Fig.12a–12b show that the specimen prepared with the optimized parameters contains numerous dense white pixels, indicating that the Fe and Mn intensities are similar over most of the field, and elemental distribution is uniform. In contrast, the specimen prepared with the higher laser power settings exhibits poor uniformity. Fig. 12c displays sparse

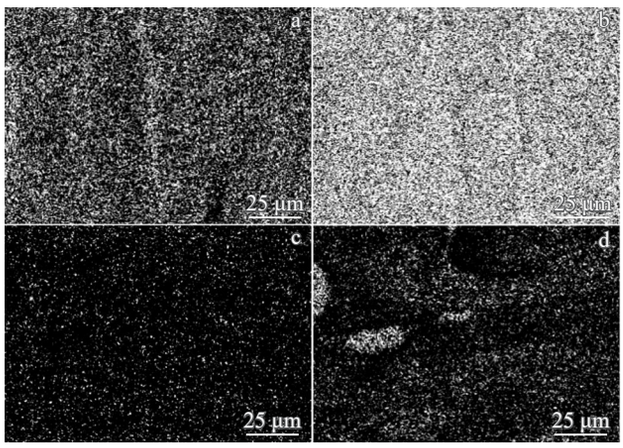


Fig.12 Transformed EDS element mappings of specimens prepared by optimized parameters (a – b) and excessively high laser energy density (c–d): (a, c) Mn; (b, d) Fe

bright pixels separated by extensive dark regions; only small and scattered Mn-rich features are present, and no large Mn-rich patches appear. This absence signifies local loss of Mn in areas, where bright Mn signals should exist. EDS element mapping of Fe in Fig. 12d differs markedly from that of Mn. Although Fe is distributed non-uniformly, isolated Fe spots are relatively few; instead, Fe-rich features are denser and coalesce into distinct bright patches, indicating Fe enrichment. The specimen contains 74.38wt% Fe and 25.62wt% Mn. This phenomenon is caused by Mn volatilization. When the laser energy density is higher (laser power is too high), the extremely high instantaneous temperature of the melt pool combined with rapid cooling causes the low-melting-point Mn to evaporate. After Mn is vaporized, its local concentration decreases, reducing EDS signal of element Mn. Consequently, after the brightness and contrast adjustments, Fig. 12c exhibits numerous dark regions. Additionally, after printing, condensed Mn powder can be found on the inner wall of the processing chamber, which further confirms the volatilization of Mn during the process. Because of the volatilization of Mn, the areas initially contain both Mn and Fe are depleted of Mn. Therefore, the remaining Fe fraction rises, resulting in local Fe enrichment. During printing, the melt pool cools rapidly. The enriched Fe has insufficient time to diffuse and homogenize, leading to the formation of Fe-rich patches observed in Fig.12d.

In summary, uniform in-situ alloying can be achieved by carefully controlling the laser processing parameters. Laser power has the greatest influence on block specimen homogeneity and should be maintained between 150–200 W. Simultaneously, the laser scanning speed should be regulated, so the volumetric energy density (VED) of the specimen, calculated using Eq. (3), falls within the range of 83–100 J/mm^3, enabling the production of fully dense (>99%) bulk samples with uniformly distributed elements. If the laser power is too low or scanning speed is overly high, elemental mixing becomes markedly non-uniform. If the laser power is excessively high, the elemental distribution is only slightly less uniform, but the overall composition of the material is noticeably altered.

$$\mathrm{VED} = \frac{P}{vht} \tag{3}$$

where P is the laser power, v is the scanning speed, h is the hatching space, and t is the layer thickness.

4.2 Effect of laser parameters on Fe-30Mn alloy properties

Laser processing parameters govern material properties by controlling the fluidity of the melt powders in the melt pool. A suitable energy density enables the molten liquid from powder melting to fill inter-particle voids more efficiently; therefore, fewer pores remain within the specimens. Consequently, the block specimen processed by optimized laser parameters has fewer defects and exhibits higher relative density, UTS, and elongation.

Specimen #1 prepared with low laser density (125 W, 800 mm/s) has many Fe-rich and Mn-rich zones and some pores, as shown in Fig. 13a. The electrochemically active Mn and adjacent Fe-rich zones create galvanic couples that accelerate dissolution of Mn-rich zones, leading to a significant increase in corrosion rate. Meanwhile, the alloy galvanic couples cause the Mn-rich zones to corrode preferentially, resulting in a sharp increase in Mn ion release. Excessive Mn ions released during specimen degradation suppress cell proliferation, ultimately increasing indirect cytotoxicity. Moreover, due to the presence of a substantial number of unmelted powder and extensive pores within the specimen #1 prepared under low energy density, the high-density internal defects result in poor UTS and elongation.

However, compared with specimen #1, when the laser power becomes higher (175 W, 800 mm/s), the corrosion rate becomes lower, and the mechanical properties become better. As shown in Fig.13b, pores are still present in the specimen #2, yet nearly no unmelted Mn particles exist, whereas unmelted Fe particles and Fe-rich zones (Fe>98wt%) can still be detected. Owing to the decreased unmelted Mn particles, the galvanic-cell effect of specimen #2 is attenuated relative to that of specimen #1, thereby lowering its corrosion rate. Concurrently, the elevated laser energy density reduces the volume fraction of unmelted powder and pores. In other words, the internal defects are reduced, so the specimen #2 exhibits superior mechanical properties compared with specimen #1.

Upon a further increment of laser energy density, all unmelted powder vanishes virtually, and internal pores are drastically decreased, leading to a pronounced increase in mechanical properties. At this time, disparities in performance are governed primarily by variations in microstructure. Fig. 13c and 13d present the microstructures of specimens #3 (250 W, 800 mm/s) and #4 (150 W, 500 mm/s), respectively. Evidently, varying mass fractions of Fe-Mn-O give rise to discernible differences in microstructure. Overall, the two specimens exhibit broadly comparable microstructure, both containing equiaxed grains (Fe:Mn<7:3), columnar grains (Fe: Mn≈7: 3), limited corrosion regions (Fe: Mn>7: 3), and dark spots, in which O content is markedly higher than that in the surrounding matrix. In contrast, spheroidal particles are

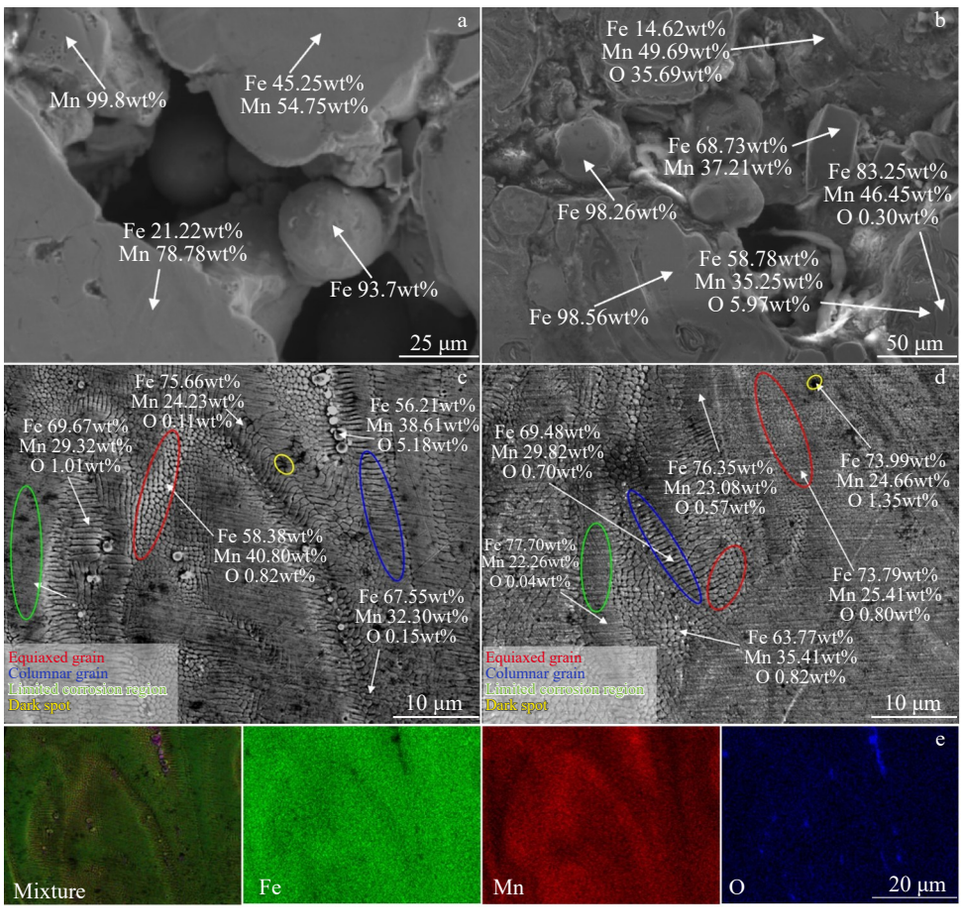


Fig.13 Surface morphologies and results of EDS analysis of specimens #1 (a), #2 (b), #3 (c), and #4 (d); EDS element mappings corresponding to Fig.13c (e)

observed on the surface of specimen #3, and corresponding EDS element mappings reveal that their O contents are approximately 5wt%, markedly exceeding that of the matrix. Concurrently, the area fraction of dark spots in specimen #3 is larger than that in specimen #4, indicating a higher O content. Furthermore, specimen #4 contains a lower fraction of columnar grain and a higher fraction of equiaxed grain. Given comparable grain sizes, the increased proportion of equiaxed grains combined with the reduced O content collectively confer on superior mechanical properties of specimen #4 relative to those of specimen #3 (Fig. 5). Generally, the anisotropic nature of columnar grains renders them more susceptible to corrosion than equiaxed grains. However, under the present Fe-Mn compositional range, the propensity for grain morphology formation varies with Fe-Mn ratio, and sometimes the Mn content in equiaxed grains consistently exceeds that in adjacent columnar grains. Under these conditions, alloy chemical composition supersedes crystallographic texture in governing corrosion behavior: the equiaxed grains with higher Mn content (Fig.13c) reduce their corrosion resistance relative to the columnar grains. Consequently, within the alloy system prepared in this study, the corrosion rate increases with the increase in Mn content. Because the overall Mn content in specimen #3 is lower than that in specimen #4, the former exhibits a correspondingly lower corrosion rate (Fig.4a–4b).

In summary, appropriate laser parameters must be selected during in-situ alloying of Fe-30Mn to prepare specimens that meet all performance requirements. In particular, low laser energy density severely degrades every key property.

4.3 Application prospects of biodegradable implants

For bone load-bearing parts, both block and Gyroid scaffold specimens exhibit good mechanical performance. For block specimen with comparable elastic modulus, its strength exceeds that of human bone (Table 3). Moreover, UTS and elongation of block specimen are higher than those of Fe-30Mn alloy prepared by powder metallurgy. The Gyroid scaffold specimen exhibits a triply periodic minimal surface (TPMS) structure with zero mean curvature, which eliminates the stress concentration commonly found in lattice structures. Its three-dimensional periodicity and excellent connectivity promote the formation of short and non-tortuous pore channels that facilitate cell ingrowth, nutrient transport, and metabolic waste removal, providing an ideal template for biomimetic applications, such as bone tissue engineering[31]. To the best of our knowledge, few previous studies have reported porous Fe-30Mn Gyroid scaffolds. This work may be the first to prepare porous Gyroid scaffolds by in-situ alloying, which simultaneously meet the elastic modulus and compressive strength requirements of both human cortical and

cancellous bone. As few studies have reported porous Fe-30Mn scaffolds prepared by additive manufacturing, Table 8 compares selected mechanical properties of the material prepared in this study with those of materials with similar composition reported in Ref. [29,32] made by SLM. Besides, the structures of the scaffold are shown in Fig. 14. Although the compressive strength of the Fe-30Mn scaffold prepared in this study is lower than that of Fe-35Mn and Fe-25Mn scaffolds, Fe-30Mn scaffold exhibits a significantly lower modulus than Fe-35Mn scaffold. Meanwhile, the maximum compressive strain of Fe-30Mn scaffold is substantially higher than that of Fe-25Mn scaffold. Considering the inherent advantages of the Gyroid structure, the results affirm the superior performance of the Fe-30Mn scaffolds prepared in this study.

This study also demonstrates that both block and porous Gyroid scaffold specimens exhibiting favorable biocompatibility and corrosion rates can be prepared by adopting suitable laser parameters. Block specimen displays indirect cytotoxicity comparable to that of pure iron without statistically significant differences (Fig. 6b), and it facilitates the growth of well-defined cellular pseudopodia (Fig. 7). Although RGR value of the Gyroid scaffold is lower than that of the pure iron block with a significant difference (Fig. 11), compared with negative control group, Gyroid scaffold specimen still meets grade 1 biosafety criteria in ISO 10993-12. Considering that RGR of pure iron blocks is less than 100%, and its surface area is much smaller than that of the Gyroid scaffold specimen, an increase in surface area may lead to the release of more harmful ions, thus further reducing RGR of pure iron block specimen. Consequently, a pure iron with Gyroid scaffold with the same shape will obtain an even lower RGR than the Gyroid scaffold specimen prepared in this study.

During long-term degradation of Fe-30Mn implants, the release of Mn ions exerts a major influence on the biocompatibility profile. Although Mn is an essential trace element for humans required by many enzymes and involved in processes such as bone formation, excessively high Mn ion concentrations can induce cytotoxicity[33]. Mn can accumulate in mitochondria, disrupt energy metabolism, and promote reactive oxygen species generation, leading to cellular oxidative stress[33]. It also activates signaling pathways, such as NF-κB and p38 MAPK, triggering inflammatory responses and cell apoptosis[34]. For the Fe-Mn alloy system, Fe and Mn form a solid solution that slows the release rate of Mn ions. Consequently, a well-alloyed Fe-Mn alloy exhibits lower cytotoxicity than pure metallic Mn[14]. Fig. 6 shows that when the laser power is lower or the scanning speed is high (Fe-Mn alloying is poor), RGR of the specimen exhibits a statistically significant difference compared with that of specimen processed with the optimal laser parameters. Combined with the results in Section 3.2.2, specimens with poorer alloying exhibit faster corrosion rates and higher release rates of Mn ion, resulting in greater biological toxicity. Interestingly, surface deposits containing Mn are observed on the corroded surface of the porous specimen in Fig. 9b. Their morphologies resemble those of hydroxyapatite formed on biodegradable bone implants. However, EDS analysis results reveal the presence of Mn in these deposits, indicating that degradation products may adsorb Mn ions, thereby potentially decreasing the concentration of Mn ions in the solution and reducing cytotoxicity during degradation. Moreover, other studies have reported that Mn-doped hydroxyapatite can enhance bone regeneration and osteogenic differentiation[35–36], suggesting that the present specimens may likewise possess the potential to promote bone growth.

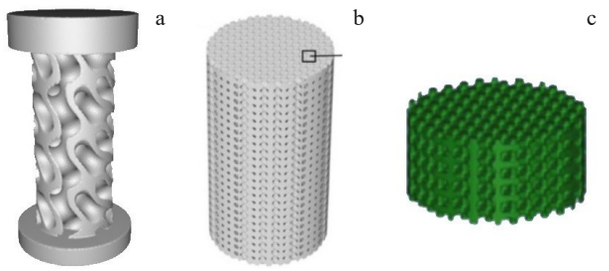


Fig.14 Schematic diagrams of scaffold structures of Fe-30Mn prepared in this study (a), Fe-35Mn[29] (b), and Fe-25Mn[32] (c)

Taken together, the Fe-30Mn alloy prepared by PBF-LB in-situ alloying has potential prospects for bone implant applications. Before further clinical application, additional experiments (e. g., in vivo toxicity and implantation studies) are still required for validation.

Table 8 Mechanical properties of different materials[29–30,32]

Material	Yield strength/MPa	Compressive strength at 20% strain/MPa	Modulus/GPa	Ref.
Fe-30Mn scaffold	66.11±1.44	170.76±8.36	6.41±0.85	This study
Fe-35Mn scaffold	89.2±1.9	304.0±7.4	33.5±1.7	[29]
Fe-25Mn scaffold	137.0±8.4	221.7±10.9*	-	[32]
Cortical bone	1–20	134+	1–35	[29–30]
Cancellous bone	7.2–23.2+	17–33+	0.02–6.00	[29–30]

Note: the symbol + indicates that the specific strain value was not provided, and the symbol * indicates that the scaffold fails at strain of 9.3%±1.5%.

5 Conclusions

1) Optimal laser parameters are essential for achieving homogeneous Fe-Mn alloy. Excessively high energy input leads to Mn evaporation, whereas insufficient energy prevents the uniform mixing of Fe and Mn. Inhomogeneous mixing produces Fe-rich and Mn-rich zones, accelerating corrosion rate, reducing mechanical properties, and increasing indirect cytotoxicity.

2) The block specimen prepared with optimal parameters exhibits relative density of 99.36%, an UTS of 644.67±12.13 MPa, the elongation of 21.61%±0.81%, a corrosion rate of 0.042 mm/a, and indirect cytotoxicity similar to that of pure iron with no statistically significant difference (RGR=105.14%±17.57% after test for 5 d).

3) The porous Gyroid scaffold specimen prepared with optimal parameters possesses a relative density of 99.41%, a yield strength specific surface area of 3031.02 mm^2/g, a porosity of 49.84%, a yield strength (0.2% offset) of 66.11± 1.44 MPa, a compressive strength of 170.76±8.36 MPa at 20% strain, an elastic modulus of 6.41±0.85 GPa, and cytotoxicity of ISO 10993-5 grade 1.

4) In summary, the above results demonstrate that the Fe-30Mn alloy prepared by PBF-LB in-situ alloying with optimal laser parameters may be a promising candidate for biodegradable bone-implant applications. Before further clinical application, additional experiments are still required for validation.

References

1 Chandra G, Pandey A. *Expert Review of Medical Devices*[J], 2021, 18(7): 629

2 Chandra G, Pandey A. *Biocybernetics and Biomedical Engineering*[J], 2020, 40(2): 596

3 Hernandez R J, Villanueva N L, Sanati-Mehrizy P *et al*. *Craniomaxillofac Trauma Reconstruction*[J], 2016, 9(2): 134

4 Alexander R, Theodos L. *Journal of Oral and Maxillofacial Surgery*[J], 1993, 51(6): 695

5 Hanson B, Werken C v d, Stengel D. *BMC Musculoskeletal Disorders*[J], 2008, 9: 73

6 Li J W, Du C F, Yuchi C X *et al*. *Journal of Medical and Biological Engineering*[J], 2019, 39(5): 633

7 Jamil W, Allami M, Choudhury M Z *et al*. *Injury*[J], 2008, 39(3): 362

8 Tsakiris V, Tardei C, Clicinschi F M. *Journal of Magnesium and Alloys*[J], 2021, 9(6): 1884

9 Al-Shalawi F D, Mohamed A A H, Jung D W *et al*. *Polymers*[J], 2023, 15(12): 2601

10 Zheng Y F, Gu X N, Witte F. *Materials Science and Engineering R: Reports*[J], 2014, 77: 1

11 Liu Y, Zheng Y F, Chen X H *et al*. *Advanced Functional Materials*[J], 2019, 29: 1805402

12 Salama M, Vaz M F, Colaço R *et al*. *Journal of Functional Biomaterials*[J], 2022, 13(2): 72

13 Rabinkin A. *Calphad*[J], 1979, 3(2): 77

14 Hermawan H, Dubé D, Mantovani D. *Journal of Biomedical Materials Research*[J], 2010, 93A(1): 1

15 Hermawan H, Purnam A, Dub D *et al*. *Acta Biomaterialia*[J], 2010, 6(5): 1852

16 Nie Y, Chen G, Peng H B *et al*. *Acta Biomaterialia*[J], 2021, 121: 724

17 Chamay A, Tschantz P. *Journal of Biomechanics*[J], 1972, 5(2): 173

18 Čapek J, Vojtěch D, Oborná A. *Materials & Design*[J], 2015, 83: 468

19 Qin Y, Wen P, Guo H *et al*. *Acta Biomaterialia*[J], 2019, 98: 3

20 Maconachie T, Leary M, Lozanovski B *et al*. *Materials & Design*[J], 2019, 183: 108137

21 Zhang Yongdi, Sun Baoyu, Wang Weizhi *et al*. *Rare Metal Materials and Engineering*[J], 2024, 53(3): 807 (in Chinese)

22 Mosallanejad M H, Niroumand B, Aversa A *et al*. *Journal of Alloys and Compounds*[J], 2021, 872: 159567

23 Sing S L, Huang S, Goh G D *et al*. *Progress in Materials Science*[J], 2021, 119: 100795

24 Endoh Y, Ishikawa Y. *Journal of the Physical Society of Japan*[J], 1971, 30: 1614

25 International Organization for Standardization. *Biological Evaluation of Medical Devices—Part 12: Sample Preparation and Reference Materials*, ISO-10993-12[S]. 2021

26 Ma X L, Hou Y Q, Liu H P *et al*. *Materials*[J], 2024, 17(9): 2029

27 Venezuela J, Dargusch M S. *Acta Biomaterialia*[J], 2019, 87: 1

28 Roesner M, Zankovic S, Kovacs A *et al*. *Journal of Functional Biomaterials*[J], 2024, 15(2): 28

29 Carluccio D, Xu C, Venezuela J *et al*. *Acta Biomaterialia*[J], 2020, 103: 346

30 Martinez-Marquez D, Delmar Y, Sun S *et al*. *Materials*[J], 2020, 13(21): 4794

31 Mall A P, Bhandarkar V V, Mandaloi G *et al*. *Archives of Computational Methods in Engineering*[J], 2025, 32(4): 2429

32 Shuai C J, Yang W J, Yang Y W *et al*. *Materials Research Express*[J], 2020, 7(1): 15404

33 Aaron B B, Gunnar F K, Elena H H *et al*. *Journal of Trace Elements in Medicine and Biology*[J], 2011, 25(4): 191

34 Prabhakaran K, Chapman G D, Gunasekar P G. *Toxicology Mechanisms and Methods*[J], 2011, 21: 435

35 Li R M, Zhu Z Y, Zhang B L *et al*. *Advanced Science*[J], 2024, 11(4): 2305890

36 Kamaraj M, Roopavath U K, Giri P S *et al*. *ACS Applied Materials & Interfaces*[J], 2022, 14(20): 23245

Fe-30Mn可降解金属的激光原位合金化及其生物学研究

汪润泽[1]，唐金成[1]，单雪鹏[1]，黄钊臻[1]，李思敬[1]，严　明[1,2]

(1. 南方科技大学 材料科学与工程系，广东 深圳 518055)

(2. 南方科技大学 嘉兴研究院，浙江 嘉兴 314031)

摘　要：利用激光束粉末床熔融（PBF-LB）原位合金化制备了块状和Gyroid多孔Fe-30Mn合金，并探讨了不同打印参数对试样性能的影响。结果表明，打印过程中激光能量密度较低会导致铁、锰元素混合不均匀，导致材料力学性能下降；激光能量密度过高则会使锰元素挥发，造成合金成分不符合预期。通过优化激光参数，可获得致密度高、铁锰元素分布均匀的试样，其抗拉强度达到644.67 MPa，延伸率达到21.61%，在模拟体液中的腐蚀速率为0.042 mm/a。此外，所得Gyroid多孔支架的孔隙率为49.84%，0.2%应变屈服强度为66.11 MPa，20%应变下的压缩强度为170.76 MPa，弹性模量为6.41 GPa。间接细胞毒性试验和细胞黏附试验结果表明，该材料具有良好的生物相容性。综上所述，本研究使用PBF-LB原位合金化制备的Fe-30Mn合金具有作为可降解人骨植入材料的应用前景。

关键词：PBF-LB；原位合金化；生物可降解金属

作者简介：汪润泽，男，2001年生，硕士生，南方科技大学材料科学与工程系，广东 深圳 518055，E-mail：12432504@mail.sustech.edu.cn